



## Facile synthesis of highly efficient ZnO/ZnFe<sub>2</sub>O<sub>4</sub> photocatalyst using earth-abundant sphalerite and its visible light photocatalytic activity

Yan Li<sup>a,1</sup>, Yanzhang Li<sup>a,1</sup>, Yidong Yin<sup>a</sup>, Dehua Xia<sup>b,c</sup>, Hongrui Ding<sup>a</sup>, Cong Ding<sup>a</sup>, Jing Wu<sup>a</sup>, Yunhua Yan<sup>a</sup>, Yi Liu<sup>a</sup>, Ning Chen<sup>d</sup>, Po Keung Wong<sup>c</sup>, Anhuai Lu<sup>a,\*</sup>

<sup>a</sup> The Key Laboratory of Orogenic Belts and Crustal Evolution, Beijing Key Laboratory of Mineral Environmental Function, School of Earth and Space Sciences, Peking University, Beijing 100871, PR China

<sup>b</sup> School of Environmental Science and Engineering, Sun Yat-sen University, Guangzhou, 510275, PR China

<sup>c</sup> School of Life Sciences, The Chinese University of Hong Kong, Shatin, NT, Hong Kong SAR, PR China

<sup>d</sup> Canadian Light Source, 44 Innovation Blvd, Saskatoon, SK, Canada



### ARTICLE INFO

#### Keywords:

ZnO/ZnFe<sub>2</sub>O<sub>4</sub>  
Natural sphalerite  
Visible light  
Photocatalytic activity  
Earth-abundant

### ABSTRACT

Micrometer-scale ZnO/ZnFe<sub>2</sub>O<sub>4</sub> coupled photocatalyst is synthesized via a simple, one-step thermal treatment performing on natural Fe-bearing sphalerite ((Zn, Fe)S). *In situ* high-temperature X-ray diffraction (XRD), thermogravimetry, differential thermal analysis (TG/DTA) and scanning electron microscopy (SEM) results indicated that octahedral ZnFe<sub>2</sub>O<sub>4</sub> (~5 μm) formed on the surface of substrate-like ZnO (tens of microns) derived from the oxidation of sulfides upon heating to 800 °C in air for 1 h, and the two components kept stable phase ratio at 3:7 (wt%) from 900 °C (sample M-900) to 1200 °C (sample M-1200). X-ray absorption spectroscopy (XAS) and Raman spectra revealed that more Zn atoms in ZnFe<sub>2</sub>O<sub>4</sub> of M-1200 occupied tetrahedral sites than M-900, resulting in a sharper A<sub>1g</sub> mode (~647 cm<sup>-1</sup>), more ordered spinel structure and less antisite defects. Compared with visible-light responsive sphalerite (Zn, Fe)S, M-1200 performed more 200 nm of red-shifted optical absorption, 2.5 times at most higher the incident photon-to-electron conversion efficiency (IPCE) and 2–3-fold photocatalytic efficiency towards degradation of methyl orange and inactivation of *Escherichia coli* K-12. Besides, the photocatalytic activities of M-1200 preponderate over M-900, typical visible-light catalyst ZnFe<sub>2</sub>O<sub>4</sub> and ZnO/ZnFe<sub>2</sub>O<sub>4</sub> mechanically mixed sample. The optimization of lattice structure and the establishment of special band alignment were suggested to be remarkably beneficial to the separation of photo-generated electrons-holes and promote the photocatalytic performance. This study would enlighten a feasible and efficient strategy to fabricate coupled photocatalyst by utilizing Earth-abundant and low-cost natural minerals for solving environmental problems.

### 1. Introduction

In 1972, Fujishima and Honda reported a pioneering work on using TiO<sub>2</sub> and UV-light to photocatalytically decompose water [1]. After that, semiconductor photocatalysis has been under extensive research and was recognized as one of the most exciting techniques towards degradation or removal of pollutants [2–5]. To date, numerous semiconducting materials have been reported as possible photocatalysts for environmental remediation. However, most of these materials possess a fairly large bandgap, resulting in limited activity under visible light irradiation. In addition, the relatively faster recombination process of photo-generated electrons and holes (~10<sup>-9</sup> s) than the surface redox kinetics (10<sup>-8</sup>–10<sup>-1</sup> s) is another dominant factor that causes low

photocatalytic efficiency [6]. Various strategies have been developed to overcome the aforementioned two limitations, two of which are synthesizing elemental doping and hybrid semiconducting materials so as to manipulate their structural, electronic and optical properties. Reports in the last two decades have indicated that the mentioned approaches not only enhance the visible light-harvesting capability, but also promote the separation of photo-generated charge carriers, thereby improving the photocatalytic efficiency.

However, the development of semiconductor photocatalysis in civil applications is still limited because most of the doped semiconductors and cocatalysts consist of expensive or scarce elements (e.g. Pt, Au, Ru, Pd, Ag, Ir and Rh) [7–12]. The fabrication of them and other multi-component hybrid semiconductors is generally a complex process

\* Corresponding author.

E-mail address: [ahlu@pku.edu.cn](mailto:ahlu@pku.edu.cn) (A. Lu).

<sup>1</sup> Equal contribution.

because a good control of the stoichiometry and phase species is challenging even in the laboratory. Therefore, in current field of environmental application, semiconductor photocatalytic technologies face increasingly competition from relatively simple physical (e.g. adsorption by zeolites and clays), chemical (e.g. Fenton reagents), and biological technologies. To become economically and technically competitive, photocatalytic technology used for civil applications must require the semiconducting materials to possess high visible light photocatalytic activity, can be mass-produced via a simple fabrication processing and are economical and environmentally friendly. The requirement is hardly met by most present semiconducting materials.

Towards this goal, natural metal oxides and sulfides minerals are two interesting candidates because most of them are visible light-responsive semiconductors and all of them are from nature [13]. In particular, ZnS, called sphalerite in mineralogy terms, is one of the most widespread ores on earth [14]. According to United States Geological Survey (USGS) data, the identified zinc resources of the world are about 1.9 billion metric tons by 2017 (<http://minerals.usgs.gov/minerals/pubs/mcs/>), and sphalerite is the chief ore of zinc and has been the principle ore mineral in the world. Nowadays, the price per ton of zinc is about 2230 dollars in London Metal Exchange (<https://www.metalprices.com/metal/zinc/lme-zinc-cash-official>), which is much lower than rare metals and noble metals. All these make it more appealing for low-cost and large-scale mass production.

Also in energy conversion and environmental related fields, we can find developing earth-abundant, low-cost and available raw materials such as natural minerals is the current trend for practical applications. For example, nature rutile ( $TiO_2$ ) was reported to photocatalytically degrade azo dyes and its efficiency was almost similar to commercial P25  $TiO_2$  [15]; Earth-abundant red phosphorous (P) was reported as a visible light-responsive photocatalyst for bacterial inactivation [16]; vermiculite as a common natural silicate mineral could generate hydrogen from photocatalytic splitting of water under visible light [17]; bornite ( $Cu_5FeS_4$ ) was used as a narrow bandgap semiconducting material with ultralow thermal conductivity applied in thermoelectric energy conversion technology [18]. From these studies, we see the natural mineral materials have a significant cost advantage over other synthetic materials in practical applications. That means it would not spend much time and money to synthesize the target materials, and the recycling use may be unnecessary because the recovery operations are time-consuming, cumbersome and high-cost as compared with direct acquisition from the nature.

We have previously investigated the semiconducting property and photocatalysis of natural sphalerite [19–25]. Stoichiometric sphalerite is cubically packed in sulfur with half the tetrahedral sites occupied by zinc. Due to the complex geological environment, natural sphalerite samples do not form perfect crystals, but always contain minor and trace elements embedded in crystal structure, presenting a variable stoichiometry [19,20]. In natural sphalerite samples, Fe and other transition metals such as Cd and Mn randomly distribute throughout the mineral by replacing Zn on lattice sites. Concentrations of impurity elements such as Fe have been observed up to 26 wt% [26]. Due to the contribution of Fe 3d orbitals to the valence band, the bandgap of sphalerite narrows with the increase of Fe content [27]. Therefore, the natural Fe-bearing sphalerite ((Zn, Fe)S), a pristine Fe-doped semiconductor, has a wide absorption in visible light region [19,20]. It has been successfully applied to reduce Cr<sup>VI</sup> [21], degrade azo dyes [22], decompose halohydrocarbons [23] and inactivate *Escherichia coli* [24,25] under visible light irradiation. However, compared with synthetic semiconductors, the photocatalytic efficiency of natural minerals remains further improvement. For example, 1 g/L natural sphalerite needs 6 h visible light irradiation to inactivate 7 Log<sub>10</sub> cfu (colony forming unit)/mL *Escherichia coli* under the optimized condition [24], while synthetic commercial  $TiO_2$  can completely inactivate *Escherichia coli* within 1 h under similar conditions except that ultraviolet light was used [28].

In geological settings, the oxidation of metal sulfides under hydrothermal and oxidizing conditions always results in the differentiation or enrichment of certain metals, therefore giving rise to paragenetic deposits of multi metal oxides. Natural sphalerite generally occurs with a certain amount of substituting Fe (at the Zn site) and is associated with pyrite ( $FeS_2$ ). The oxidation of the sulfide ore will generate paragenetic zincite ( $ZnO$ ) and franklinite ( $ZnFe<sub>2</sub>O<sub>4</sub>$ ) [29,30]. It should be noted both  $ZnO$  and  $ZnFe<sub>2</sub>O<sub>4</sub>$  are semiconductors. The synthetic coupled  $ZnO/ZnFe<sub>2</sub>O<sub>4</sub>$  in laboratory have been demonstrated to exhibit remarkably enhanced photocatalytic activity by generating *n-p* heterojunction and inhibiting the recombination of photo-generated electron-hole pairs [31–34]. However, these synthetic methods require major expenditure of time and steps, therefore can't achieve the demand of energy conservation or easily bring in secondary pollution.

This study is dedicated to developing coupled  $ZnO/ZnFe<sub>2</sub>O<sub>4</sub>$  semiconductor from natural Fe-bearing sphalerite by a simple, template-free and one-step thermal treatment. The samples were characterized by *in situ* high-temperature X-ray diffraction (XRD), thermogravimetry and differential thermal analysis (TG/DTA), environmental scanning electron microscopy (ESEM), X-ray absorption spectroscopy (XAS), Raman spectra, UV-vis diffuse reflectance spectra (DRS), photoluminescence (PL) spectra and photoelectrochemistry measurement. The synergistic effect of the newly fabricated  $ZnO/ZnFe<sub>2</sub>O<sub>4</sub>$  photocatalyst was examined and compared with natural sphalerite, pure  $ZnO$ ,  $ZnFe<sub>2</sub>O<sub>4</sub>$  as well as  $ZnO/ZnFe<sub>2</sub>O<sub>4</sub>$  mechanical mixture samples by photocatalytic inactivation of *Escherichia coli* and degradation of a model dye pollutant methyl orange (MO) in visible light. This work would contribute to the large-scale mass production and simple fabrication processing of visible light-responsive photocatalysts. It is also possible and applicable to extend this method to fabricate other hybrid semiconductors.

## 2. Materials and methods

### 2.1. Materials

The natural sphalerite sample used in our experiment was collected from a lead-zinc deposit in Yunnan Province, China. After gravitational separation and flotation, the sphalerite powder sample was heated in 900 °C and 1200 °C separately under air atmosphere for 1 h, using a high-temperature box resistance furnace with a 5 °C/min heating rate, and then quenched in cool water. The natural sample and the thermal modified samples were named as M-0, M-900 and M-1200, respectively. All of them were ground into powder and then sieved into 340 mesh size grain, i.e. the particle size was less than 40 µm. For comparison, three standard samples including pure  $ZnO$ ,  $ZnFe<sub>2</sub>O<sub>4</sub>$  and their mechanical mixture were prepared. Commercial  $ZnO$  as well as all chemicals used in this study are A.R. (analytical reagent) grade, purchased from Sinopharm Chemical Reagent Beijing Co., Ltd.  $ZnFe<sub>2</sub>O<sub>4</sub>$  powder was thermally synthesized through the conventional solid-state reaction: the mixture of  $Fe_2O_3$  and  $ZnO$  with 1:1 molar ratio was sintered at 900 °C for 15 h in air and then cooled to room temperature at a rate of about 110 °C/h. The mixed sample was obtained from the uniform blend of  $ZnO$  and  $ZnFe<sub>2</sub>O<sub>4</sub>$  in 7:3 mass ratio, which was referred to the component of M-900 and M-1200 based on XRD quantitative result.

### 2.2. Characterization methods

*In situ* high-temperature X-ray diffraction (XRD) was carried out in the temperature range of 27–1160 °C at regular intervals of 50 °C in air atmosphere, using an X-ray diffractometer (X'pert Pro MPD, PANalytical, Netherland) equipped with Cu K $\alpha$  irradiation ( $\lambda = 1.5406 \text{ \AA}$ ) and a high temperature heating stage. A heating rate of 1 °C/min and a holding time of 30 min before scanning at each temperature of measurement were maintained. The patterns were recorded from 22 to 85° (2θ) and the scanning speed was 0.5°/min at 40 kV, 100 mA. According to the method of QPA (quantitative phase analysis)

in GSAS software package, the quality percentages of different phases were obtained [35,36]. XRD patterns of M-900 and M-1200 were recorded using the same instrument and condition except performing at room temperature. Simultaneous thermal-gravimetric analysis and differential thermal analysis (TG/DTA) were carried out with a thermogravimetric apparatus (Q600SDT, Thermal, USA). The heating rate was 10 °C/min up to 1200 °C in a dynamic air atmosphere. X-ray absorption spectroscopy (XAS) measurements at Zn K-edge in transmission mode was performed at the 4W1B beamline in Beijing Synchrotron Radiation Facility (BSRF). The electron beam energy was 3.5 GeV and the stored current was 260 mA (top-up). XAS data were collected using a fixed-exit double-crystal Si (111) monochromator and the energy was calibrated using Zn foil. The spectra were calibrated, averaged, pre-edge background subtracted, and post-edge normalized using Athena program in IFEFFIT software package [37]. The room temperature Raman spectra of samples were recorded on a Microscopes Raman Spectrometer (inVia Reflex, RENISHAW, UK) in the range 50–800 cm<sup>-1</sup> with the resolution of 1.2 cm<sup>-1</sup>, using the 532 nm line as excited laser and the average power reaching sample surface was about 2 mW. UV-vis diffuse reflection spectrum (DRS) were collected using a UV-3600 Plus UV-vis spectrophotometer with an integrating sphere from 300 to 800 nm. The slit width was 2.00 nm and BaSO<sub>4</sub> (A.R., analytical reagent) was used as the reference. The powder of sample was dispersed ultrasonically in ethyl alcohol and then a few drops of suspension were loaded on a clean Si substrate. After that, the prepared sample with substrate was carried out the micromorphology observation and photoluminescence (PL) measurement. The micromorphology was observed by environmental scanning electron microscopy (ESEM, Quanta 200FEG, FEI) with an accelerating voltage of 15.0 kV and 4.0 μm beam size. The PL spectra were recorded at room temperature using a home-assembled system equipped with SP-2500 spectrophotometer (Princeton Instruments, USA) and 532 nm solid-state laser. The intensity of the excitation light was around 1 W/μm<sup>2</sup> with 1 μm beam size and wavelength resolution could reach ± 0.4 nm.

### 2.3. Photoelectric response measurement

In the electrochemical system, a quartzy cell was equipped three-electrode configuration consisting of 70 mL 0.5 M NaSO<sub>4</sub> and 0.5 M ethanol electrolyte. A glassy carbon electrode filmed by mineral photocatalyst, a platinum foil and a saturated calomel electrode (SCE, 0.242 V corrected to a normal hydrogen electrode (NHE)) served as the working electrode, counter electrode and the reference electrode, respectively. An external voltage (−0.5 V vs. SCE) was applied and the generated photocurrent was recorded using a CHI model 660 °C potentiostat (Shanghai Chenhua Instruments Corporation, China). The light of xenon lamp ( $\lambda > 400$  nm, Perfect Light, China) passed through a series of monochromatic light filters and reached the cell, whose intensity was measured by a UV radiometer (made in the Photovoltaic Instrument Factory of Beijing Normal University). The working electrode was prepared as follows: 10 mg photocatalyst powder was dispersed into 0.5 mL 4:1 water ethanol mixture and then 20 μL of the suspension was dripped onto the glassy carbon substrate. The electrode was available when it got dry.

The incident photon-to-electron conversion efficiency (IPCE) values, namely the number of photoelectrons generated in the external circuit divided by the number of photons received on the mineral surface, were calculated for each wavelength according to Eq. (1) [38].

$$\text{IPCE}(\%) = N_e/N_p = \frac{ihc}{\lambda Pe} \times 100 \quad (1)$$

where  $i$  is the photocurrent density,  $h$  is Planck's constant,  $c$  is velocity of light,  $P$  is the incident light power density,  $\lambda$  is monochromatic light wavelength, and  $e$  is the elemental charge.

## 2.4. Photocatalytic reactions

### 2.4.1. Degradation of azo-dye

Since methyl orange (MO) dye is a model compound that is commonly used in many studies, the photocatalytic degradation of MO was employed here to measure the photocatalytic activity of the photocatalyst under ambient environment. The photocatalyst powder (0.5 g/L) was dispersed by a stirrer in 100 mL aqueous solution containing MO ( $6 \times 10^{-5}$  mol/L) and ascorbic acid (0.08 mol/L) as the reactant and hole-scavenger, respectively. The pH of the suspension was kept at  $3.2 (\pm 0.2)$  by ascorbic acid/sodium ascorbate buffer solution. Irradiation was provided by a 500 W long-arc xenon lamp ( $\lambda > 400$  nm, Perfect Light, China), which was placed 9 cm away from the reactor. The average light intensity striking the reactor was about 21 mW/cm<sup>2</sup>, measured by a UV radiometer (made in the Photovoltaic Instrument Factory of Beijing Normal University). After a certain period of irradiation, 1.0 mL suspension was extracted from each reaction system and filtered out powder, followed by taking the supernatant solution to measure the adsorption spectra of MO at 504 nm by UV-Vis spectrophotometer (Thermo Fisher Scientific, USA). Additional two parallel groups and blank group without photocatalyst were carried out simultaneously.

### 2.4.2. Bacterial inactivation

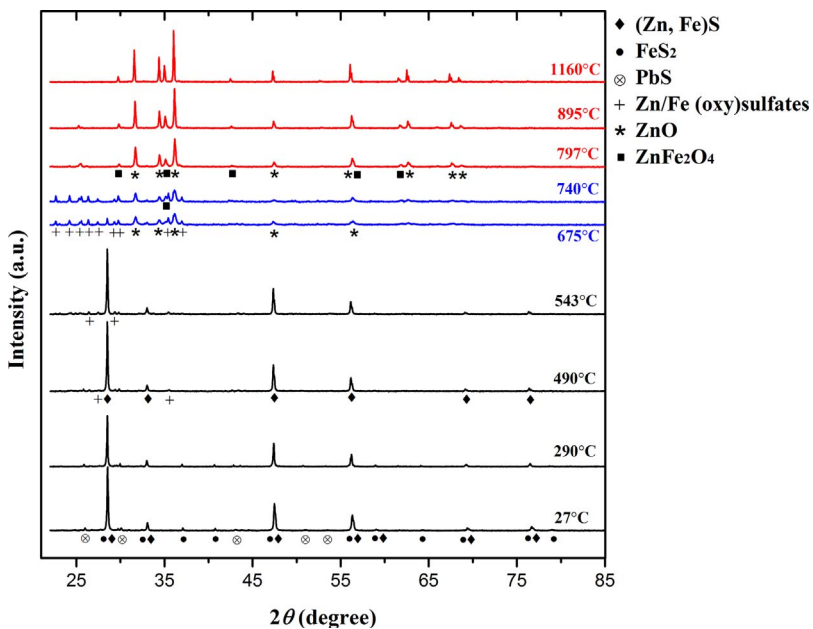
*Escherichia coli* K-12, a representative Gram-negative bacterium, commonly used as a faecal contamination indicator microorganism, was chosen as model bacterium for measuring the photocatalytic disinfection effect of the photocatalyst. A 400 mL suspension (pH = 6.8) containing 0.4 g catalyst and  $10^7$  cfu/mL *E. coli* K-12 in a flask was placed in a black box and vigorously stirred at suitable velocity. The fluorescent tubes (15 W, VELOX, Thailand) were applied as light source and placed in the back side of the reactor with a liquid filter (5 mol/L sodium nitrite) to block all ultraviolet light emission. The intensity of visible light was 3.3 mW/cm<sup>2</sup> and no UV light was detected according to a light meter (LI-COR, Lincoln, Nebraska, USA) and an UVX digital radiometer (UVP, Upland, California, USA), respectively. At regular intervals, stirring was stopped first, then aliquots of the sample were collected and serially diluted with sterilized saline (0.9% NaCl) solution. 0.1 mL of the diluted sample was immediately spread on nutrient agar (Lab M, Lancashire, UK) plates and incubated at 37 °C for 24 h to determine the survival number of cells (in cfu) by plating them on agar plate.

## 3. Results and discussion

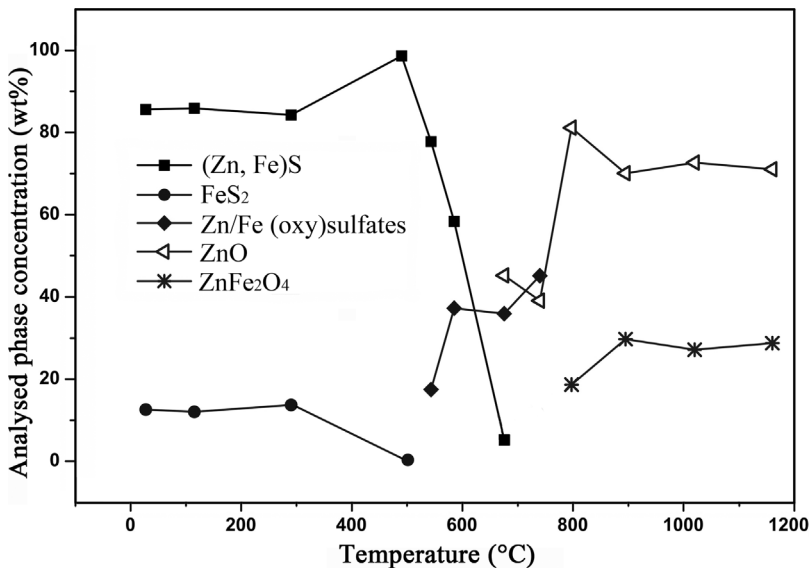
### 3.1. Thermochemistry reactions and phase changes

Fig. 1 shows the *in situ* XRD patterns of the natural sample M-0 heated at measured temperature of 27 °C, 290 °C, 490 °C, 543 °C, 675 °C, 740 °C, 797 °C, 895 °C and 1160 °C, respectively. For M-0 at room temperature, a trace amount of gelenite (PbS) is detected but its diffraction peaks are observed to be just slightly higher than the baseline, so it would not be discussed since its negligible content. The rest diffraction peaks can be assigned to two major mineral phases: cubic sphalerite (ZnS) (as indicated by the three strongest characteristic peaks at  $2\theta$  of 28.9°, 48.1° and 57.1°, JCPDS card no. 80-0020) and cubic pyrite (FeS<sub>2</sub>) (as indicated by the three strongest characteristic peaks at  $2\theta$  of 33.1°, 37.2° and 56.4°, JCPDS card no. 42-1340). And the quality percentages of sphalerite and pyrite are calculated to be 86% and 14%, respectively, according to the QPA result. It is noted that sphalerite samples used in our research contain 3% (wt%) Fe, which partly substitutes for Zn to generate the binary sulfide in the form of solid solution [23]. Thus, the chemical formula of sphalerite can be given as (Zn, Fe)S.

Based on the variations of the mineral phases, the whole heating process can be divided into four key stages: (1) 27–490 °C: The change in this stage is incredibly tiny except a slight shifting of the peaks due to



**Fig. 1.** *In situ* high temperature XRD patterns of M-0 sample calcined from the room temperature to 1200 °C with proper interval.



**Fig. 2.** The phase ratio variation during the *in situ* heating process according to the method of QPA (quantitative phase analysis) in GSAS software package.

the thermal effect, suggesting (Zn, Fe)S and FeS<sub>2</sub> keep steady in this temperature range. (2) 490–675 °C: At 490 °C, a small quantity of zinc oxysulfate ( $\text{Zn}_3\text{O}(\text{SO}_4)_2$ ) phase (JCPDS card no. 71-2475) begins to form, along with the disappearance of FeS<sub>2</sub>. At the same time, some Fe-bearing sulfates with a low amount and poor crystallinity begin to emerge, such as ferrous sulfate ( $\text{FeSO}_4$ ) [39], ferric sulfate ( $\text{Fe}_2(\text{SO}_4)_3$ ) [40] and ferric oxysulfate ( $\text{Fe}_2\text{O}(\text{SO}_4)_2$ ) [41]. Their diffraction peaks might be covered by those of  $\text{Zn}_3\text{O}(\text{SO}_4)_2$ , which results from their chemical composition and crystal structure are similar to each other. (3) 675–797 °C: The initial reactant (Zn, Fe)S completely gets involved in the thermal reactions and is oxidized to generate zincite (ZnO) and  $\text{Zn}_3\text{O}(\text{SO}_4)_2$ . Notably, the diffraction peaks of zinc/iron oxysulfate and sulfate are broad with undesirable signal-to-noise ratio, implying they have poor crystallinity and are likely nanoscale. In addition, a trace fraction of franklinite ( $\text{ZnFe}_2\text{O}_4$ ) appears at 740 °C and indicates that Zn and Fe are going to assemble together. (4) 797–1160 °C: In this temperature range, intermediate product zinc/iron oxysulfate and sulfate disappear, and ZnO and ZnFe<sub>2</sub>O<sub>4</sub> become the final stable phases. Their peaks go sharper with elevated temperature, indicating the mineral crystallinity gets better under thermal effect. Fig. 2 illustrates the phase

ratio variation during the heating process based on quantitative analysis of XRD, which accords well with above discussion. We can find that ZnO and ZnFe<sub>2</sub>O<sub>4</sub> become the main mineral phases above 900 °C and keep a relatively constant phase ratio of 70% and 30%, respectively.

To further understand the thermochemical process of the phase change reactions, TG/DTA measurements were conducted (Fig. 3) and analyzed by combining with the *in situ* XRD results. Before 500 °C, the small loss (4%) of weight accompanied with an endothermal valley at 128 °C is arisen from the evaporation of absorbed water on mineral surface. Particularly, a significant endothermal valley appearing in the range of 500–600 °C could be attributed to (Zn, Fe)S and FeS<sub>2</sub> begin to react and produce oxysulfates and sulfates. Within the temperature range of 650–800 °C, there is only an endothermal slope and a tiny valley as well as successive weight loss. Based on *in situ* XRD results, we attribute this stage to the slow decomposition of  $\text{Zn}_3\text{O}(\text{SO}_4)_2$  and the formation of ZnO. The continuous decrease in weight between 500 and 800 °C is correlated to the outgassing of sulfur compound, mainly in the form of  $\text{SO}_3$  according to previous researches on heating and oxidation of sulfide and oxysulfate [42,43]. In the last stage, the endothermic

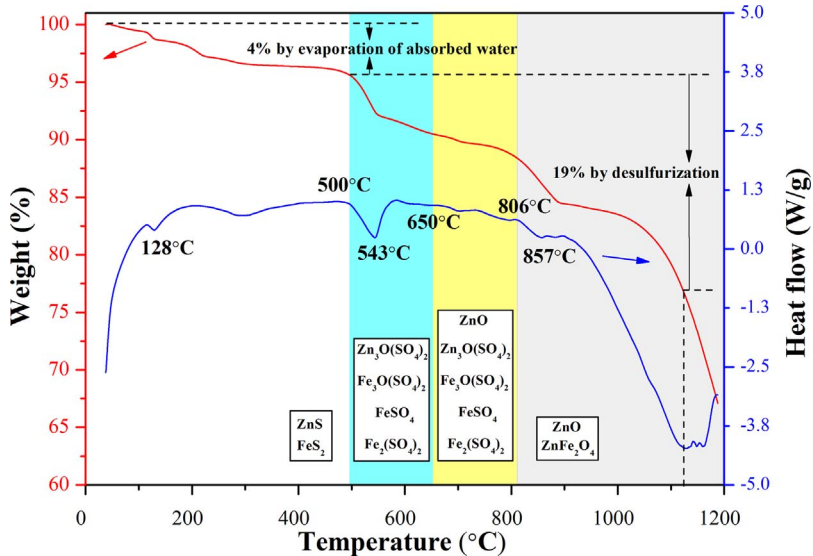


**Fig. 3.** DT (blue line) and TG (red line) curves of M-0 sample calcined from the room temperature to 1200 °C. The thermal process is divided into four stages (shown as different colors) based on component phases. (For interpretation of the references to color in this figure legend, the reader is referred to the web version of this article.)

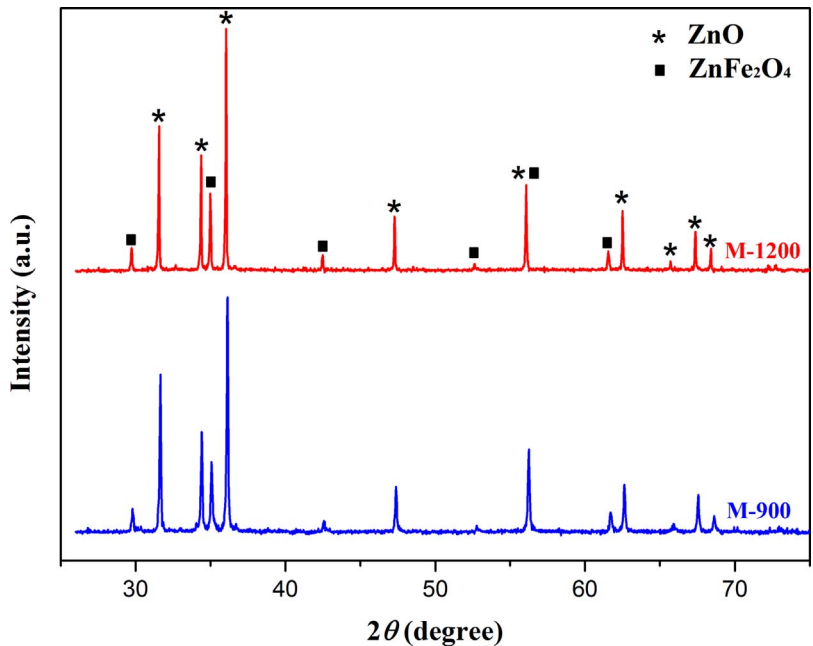
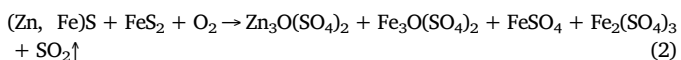


**Fig. 4.** XRD patterns of M-900 and M-1200. The assignments of diffraction peaks to ZnO and ZnFe<sub>2</sub>O<sub>4</sub> are labeled as asterisk and square, respectively.

feature starting from 806 °C and centering at 857 °C corresponds to the massive formation of ZnFe<sub>2</sub>O<sub>4</sub>. When the temperature exceeded 900 °C, we notice a huge weight loss and a dominant endothermal phenomenon, which is interpreted as a further desulfurization. The endothermal process stops at 1100 °C and the total weight loss during the desulfurization is 19%. This value accords well with the theoretical estimation of the weight loss in the reaction equations that ZnS (86%) and FeS<sub>2</sub> (14%) are completely oxidized and converted into ZnO and ZnFe<sub>2</sub>O<sub>4</sub>. Based on the above analysis, the main reactions of the heating process and their initial reaction temperature can be presented as Eqs. (2)–(4).

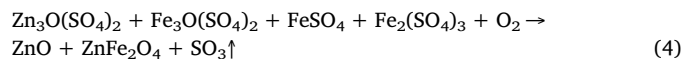
At 500 °C:



At 650 °C:



At 800 °C:



Another *ex situ* XRD measurement aims at the identify of M-900 and M-1200 that the thermally-treated and quenched samples of M-0 in 900 °C and 1200 °C for 1 h, as shown in Fig. 4. As expected, the patterns and quantitative results are exactly the same with that of *in situ* thermal XRD at corresponding temperature. Therefore, M-900 and M-1200 can represent the high-temperature phase of M-0 for following investigation. It shows that the diffraction peaks emerged in M-900 are generally broader than those in M-1200, implying the degree of crystallinity, to some extent, the particle size of the former is smaller than the latter. Fig. 5(a) and (b) display ESEM morphology of M-0 and M-900, and Fig. 5(c)–(f) shows ESEM morphology and EDS elemental analysis of the M-1200. Specifically, M-0 presents massive, fragmentary and irregular particles from several hundred nanometers to ten micrometers, indicating its crude and pristine feature. When calcined in 900 °C and 1200 °C, the generated particles possess more smooth and flatter surface which is attributed that crystals go through the nucleation and growth process under thermal effect. Notably, M-900 exhibits the similar grain

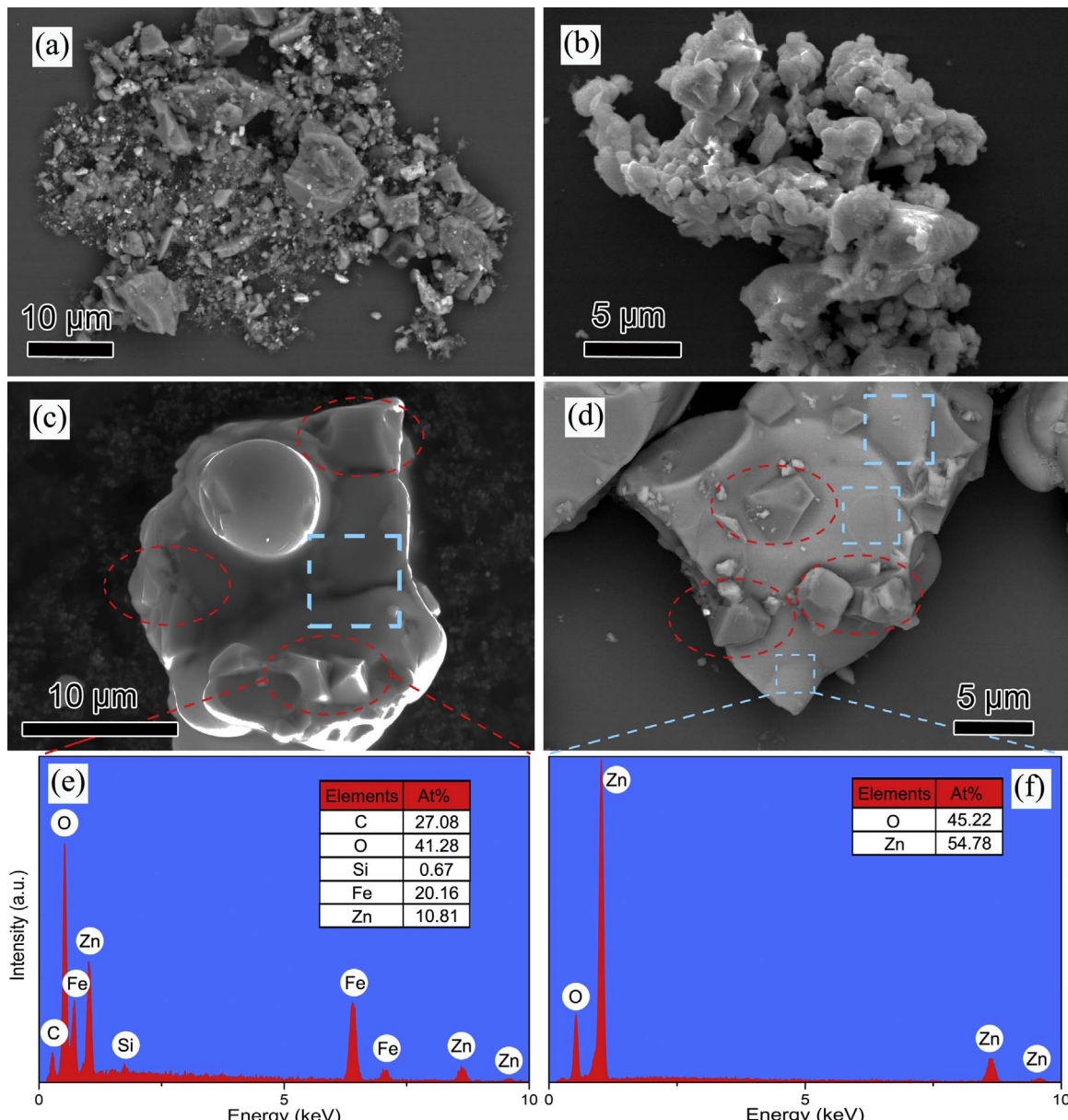


**Fig. 5.** The ESEM images of (a) M-0, (b) M-900 and (c), (d) M-1200. ZnO and ZnFe<sub>2</sub>O<sub>4</sub> in (c) and (d) are labeled as dotted blue squares dotted red ellipses, respectively. (e) EDS spectrum of ZnFe<sub>2</sub>O<sub>4</sub> octahedron and its elemental analysis listed in inset table. (f) EDS spectrum of substrate-like ZnO and its elemental analysis listed in inset table. (For interpretation of the references to colour in this figure legend, the reader is referred to the web version of this article.)

size as M-0 while M-1200 is significant larger and has no more any nanoparticle, which suggests that mature crystals formed in 1200 °C are the production of agglomerating with high crystallinity and further validates the inference from XRD. It is observed that there are two types of crystals in M-1200, one of which with bigger size serves as the substrate and the other with a typical octahedral shape is embedded in the surface of substrate-like crystals. The EDS results show the atomic ratio of Zn and O in substrate-like crystals (indicated by red ellipses) is around 1:1, and Zn, Fe, O in the octahedral crystals (indicated by blue aquares) is around 1:2:4, which are assigned as ZnO and ZnFe<sub>2</sub>O<sub>4</sub>, respectively. The cubic-symmetric ZnFe<sub>2</sub>O<sub>4</sub> particles with octahedral shape and ideal crystalline form should be the mature production of crystal growth at high temperature. During the calcining process, iron in (Zn, Fe)S was reported to be apt to outwards migrate to surface from internal lattice [30,44], moreover, the fusion of minor iron (oxy)sulfates and zinc oxyxsulfate must be less than that of major zinc oxyxsulfate particles themselves, giving rise to the observation that ZnFe<sub>2</sub>O<sub>4</sub> particles embedded in the surface of substrate-like ZnO. The two phases

almost grow together and are closely integrated with each other, which is highly favorable to the conduction of charges between them and development of coupled semiconductor. Consistently, the Electron Microprobe Analysis (EMPA) of M-1200 also corroborates the existence of this two crystal phases and discovers a few amounts of Fe in ZnO and Cu, Mn, Pb in ZnFe<sub>2</sub>O<sub>4</sub> (Table SI in Supplementary Information).

### 3.2. Optical absorption analysis

The optical properties of M-0, M-900 and M-1200 are investigated by UV-vis DRS, as shown in Fig. 6. The darker color of M-1200 implies a more remarkable ability to absorb visible light as compared with M-0 and M-900 (Inset in Fig. 6). All samples exhibit strong absorption in the whole range of visible light. Specifically, M-0 has a broad absorption shoulder band in the region of 420–600 nm, which is due to the existence of impurity levels derived from isomorphous substitutions by foreign ions [19]. As compared with M-0, the DRS absorption edge of M-900 and M-1200 shows an obviously red shift. The maximum

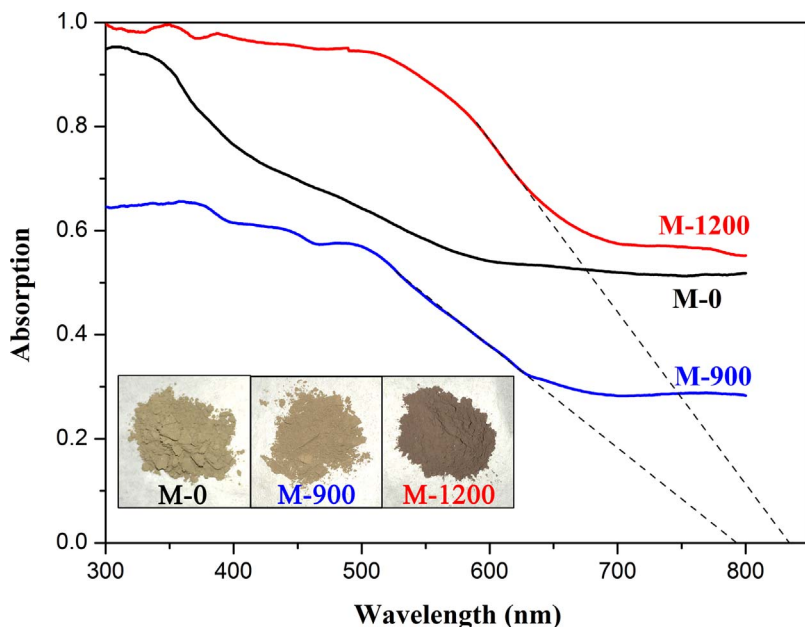


**Fig. 6.** UV-vis DRS of sample M-0, M-900 and M-1200. Insets show the color contrast of the powder samples.

absorption wavelength of M-900 and M-1200, determined by linear extrapolation, can reach at 790 nm and 830 nm, suggesting their estimated optical bandgap ( $E_g$ ) values are around 1.6 eV and 1.5 eV, respectively. Such narrow band-gap values would not belong to ZnO, whose optical band-gap value is supposed as 3.2 eV and absorption spectrum should be overlapped by ZnFe<sub>2</sub>O<sub>4</sub> [45]. The  $E_g$  value of pure ZnFe<sub>2</sub>O<sub>4</sub> is 1.9 eV, corresponding to the absorption edge of 653 nm [46]. Obviously, there is a red shift of absorption edges for ZnFe<sub>2</sub>O<sub>4</sub> in M-900 and M-1200 compared with pure ZnFe<sub>2</sub>O<sub>4</sub>, which may be attributed to the minor impurities in ZnFe<sub>2</sub>O<sub>4</sub> (such as Cu, Mn and Pb, shown in Table S1) altered the electronic structure and narrowed the optical band gap [47,48].

### 3.3. Visible-light photocatalytic activity

Fig. 7(a) shows the degradation of MO in visible light when ZnO, ZnFe<sub>2</sub>O<sub>4</sub>, mixed ZnO/ZnFe<sub>2</sub>O<sub>4</sub>, M-0, M-900 and M-1200 were separately added into MO solution. It is found that ZnO, mixed ZnO/ZnFe<sub>2</sub>O<sub>4</sub> and ZnFe<sub>2</sub>O<sub>4</sub> induce 39%, 32% and 8% of decoloration at first 10 min while later all exhibit a slow removal rate with the same rate as direct photolysis (blank group). We conclude this to an initial physical adsorption by powder surface and a followed photodissociation of MO, that is, the degradation process assisted by these photocatalysts seems negligible in this condition. Notably, the commercial ZnO plays an essential role in adsorbing MO molecules, which might be ascribed to its nanometer feature and numerous adsorption sites, while pure ZnFe<sub>2</sub>O<sub>4</sub> seems to be out of work in such condition. With photolysis only, the above four systems need more than 12 h to thoroughly eliminate MO (not shown). Unlike above substances, M-0, M-900 and M-1200 surely perform visible light photocatalytic activity. Among them, about 25% MO is removed by both M-0 and M-900 after 60 min and its complete degradation require 200 min and 180 min, respectively (not shown). In contrast, M-1200 can remove 95% MO after only 60 min of irradiation, displaying a significant enhancement in photocatalytic activities. Interestingly, we can find that the MO degradation efficiency by M-1200 is twice higher than M-900 although they have the same assembled phases, and also remarkably preponderates the mixture sample that possesses equivalent components.

The other experiments aim at comparing the photocatalytic efficiency on the disinfection of *E. coli* K-12. As shown in Fig. 7(b), all powder samples more or less exhibit the inhibition effect towards bacterial activities under visible light whereas direct photolysis of *E.*

*coli* K-12 without any powder is negligible (not shown). In particular, the *E. coli* K-12 bacterial population decreases with time until they are completely inactivated at 3 h by M-1200. By contrast, M-900 needs 5 h and M-0 needs more than 6 h to achieve this goal. Notably, a boost of disinfection rate in M-0, M-900 and M-1200 systems respectively appear after 4 h, 3 h and 1 h, at which might be the saturation of adsorption capacity and following dominant photocatalysis. As for pure samples, ZnFe<sub>2</sub>O<sub>4</sub> displays similar performance as M-900 in first 4 h but shows an obvious slowdown later, and it takes more time than M-0 to eliminate *E. coli* K-12 (not shown). Such a turning point, by making comparison to the above systems, might be attributed to an initial prominent physical adsorption and subsequent minor photocatalytic inactivation. Pure ZnO, by comparison, behaves the unsatisfactory slowest inactivation rate that merely causes very slight reduction of cell density after 6 h. Similar to MO degradation, we conclude this to the huge specific surface area of commercial ZnO and its ultraviolet-light responsive feature. It should be pointed out that the ZnO and ZnFe<sub>2</sub>O<sub>4</sub> mixed sample can totally inactivate 7-log<sub>10</sub> cfu/mL *E. coli* K-12 after 4 h irradiation, whose efficiency is even higher than M-0 and M-900. According to the above discussion, it is probably ascribed to the combined effect of adsorption from the two components and tiny photocatalysis from ZnFe<sub>2</sub>O<sub>4</sub>. Obviously, M-1200 displays the highest photocatalytic disinfection activity, which is similar to the situation of MO degradation. Compared with the mechanical mixed sample, obvious enhancement of bacterial inactivation rates for M-1200, exhibited after 1 h irradiation, is due to crystal intergrowth of ZnO and ZnFe<sub>2</sub>O<sub>4</sub>, and more importantly, formation of stable coupled-semiconductor system.

Based on the above experimental results, it is apparent that M-1200 shows the best photocatalytic performance among all samples, especially contrast with M-900 and M-0. Therefore, further investigation should be focused on 1) why the photocatalytic performance of M-900 is not as prominent as M-1200 although they have same phases, alike absorbance and similar particle size, and 2) how does M-1200 work on improving the photocatalytic activity as compared with M-0.

### 3.4. Lattice structure impacts on photocatalytic activity

As is well-known, a successful photocatalytic process benefits from three issues of crucial importance: 1) generation of excited charges (photo-generated electrons and holes), 2) separation and migration of excited charges, and 3) charges are trapped by proper target molecules on surface. Although both M-1200 and M-900 are identified with the

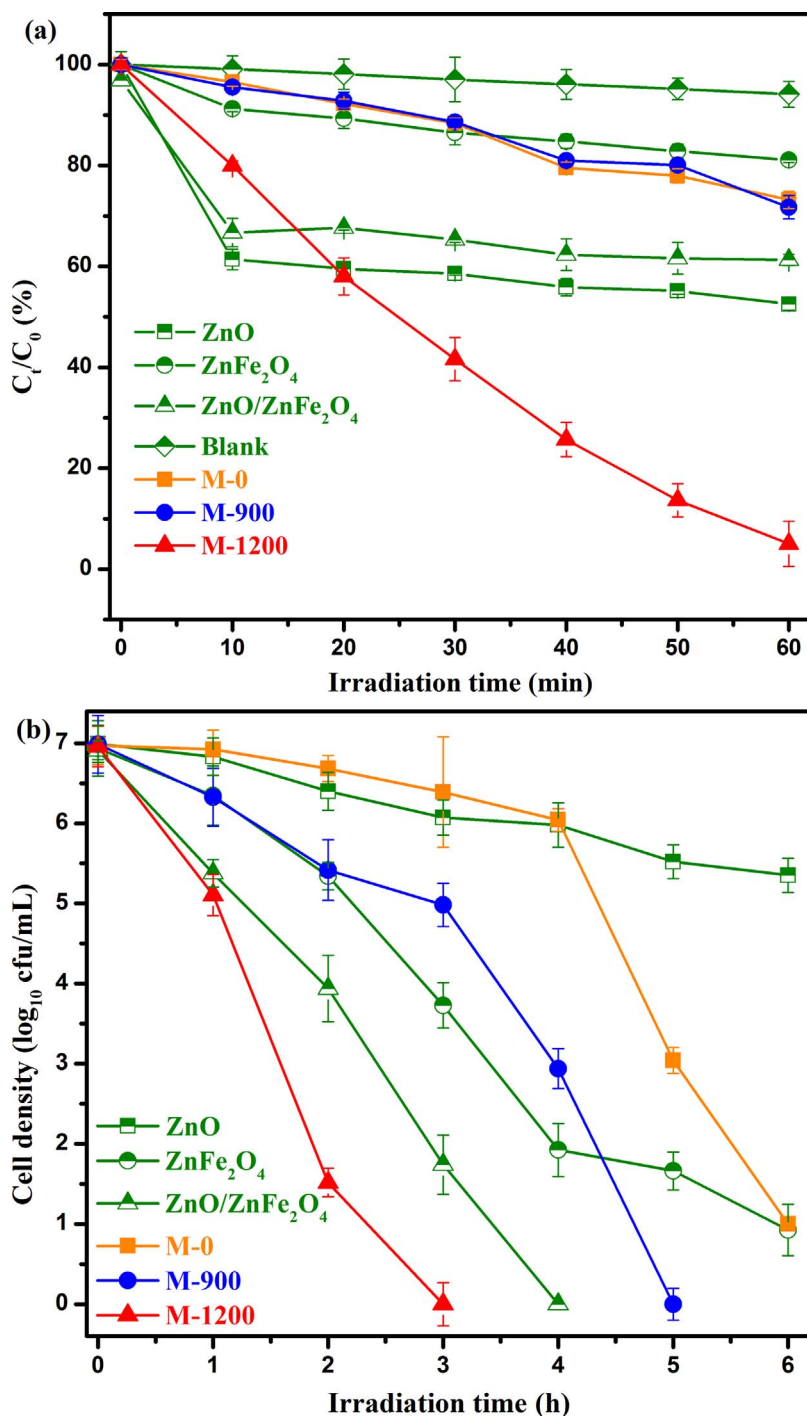
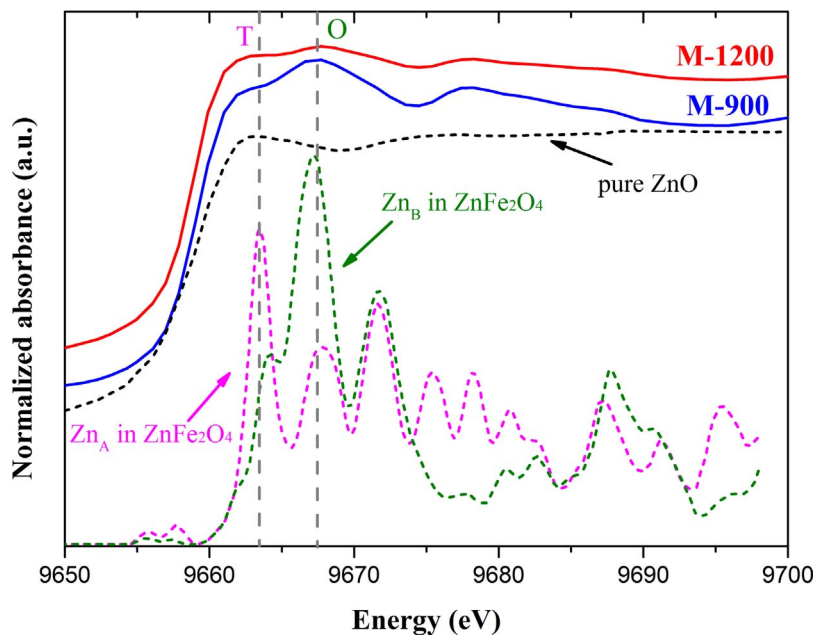


Fig. 7. Photocatalytic activities of M-0, M-900 and M-1200 samples as well as pure ZnO, ZnFe<sub>2</sub>O<sub>4</sub>, ZnO/ZnFe<sub>2</sub>O<sub>4</sub> mixture under visible light irradiation. (a) Degradation of MO; (b) Disinfection of *E. coli* K-12.

same mineral components and are visible light photo-responsive, they perform very different photocatalytic activity. Excluding other factors, such as chemical composition, component, particle size and photo-response, it may be attributed to the structural changes induced by high temperature. As indicated by TG/DT analysis (Fig. 3), thermal reactions are still in progress during 800–1200 °C. Moreover, M-900 and M-1200 show room-temperature ferromagnetism and paramagnetism, respectively (Fig. S1 in Supplementary Information). And for all we know that the pure ZnO would not give rise to magnetic moment because the outer-most electronic shells of zinc ions are fully occupied. Thus the different magnetic performances should be ascribed to thermally-related structural change in ZnFe<sub>2</sub>O<sub>4</sub> spinel, which is originated from cation configuration over the tetrahedral and octahedral sites [49–51].

In order to investigate the structural changes at high temperature, XAS and Raman spectra tests were conducted on samples M-900 and M-1200.

In equilibrium state of ZnFe<sub>2</sub>O<sub>4</sub>, Fe and Zn atoms are surrounded by octahedral (B) and tetrahedral (A) oxygen arrays, respectively, called ordered or normal spinel structure [49,50]. The formation of inverse spinel structure is induced by disorganized distribution of Fe and Zn atoms, which can be deemed as a type of antisite defect [51] and be detected by sensitive XAS technique. Fig. 8 illustrates the experimental and theoretical Zn *K*-edge XANES spectra. The theoretical Zn *K*-edge XANES of spinel ZnFe<sub>2</sub>O<sub>4</sub> (see pink and green dashed lines in Fig. 8) consists of two resolved peaks at around 9663 (peak T) and 9667 eV (peak O) as well as other peaks at higher energy [49]. The characteristic



**Fig. 8.** Zn K-edge XANES spectra of M-900 and M-1200. The pink and green dashed lines are theoretical spectra of Zn in the tetrahedral site and the octahedral site, respectively [49], and the black dashed line is the experimental spectrum of pure ZnO. (For interpretation of the references to colour in this figure legend, the reader is referred to the web version of this article.)

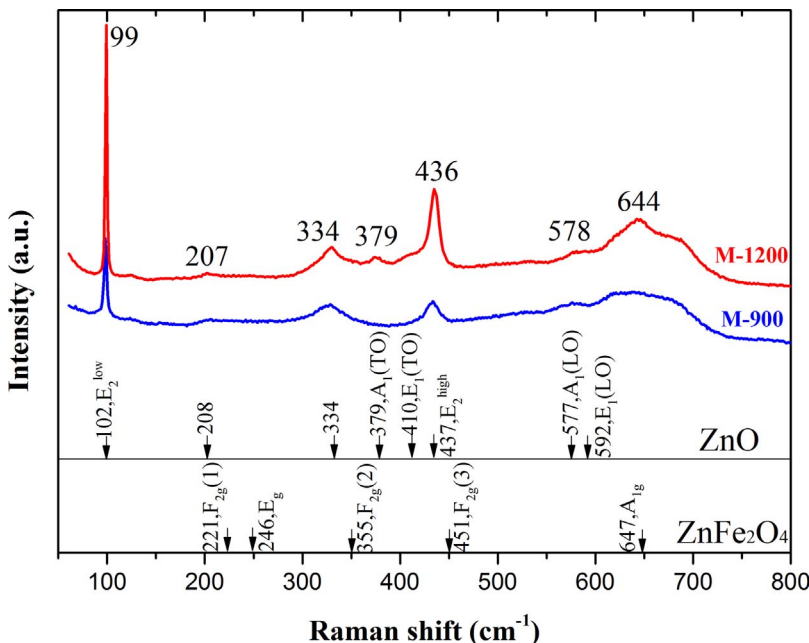


**Fig. 9.** Raman spectra of M-900 and M-1200 samples, as well as the vibration modes of ZnO and ZnFe<sub>2</sub>O<sub>4</sub> cited from reference [52–55].

peak T and peak O represent that Zn atoms occupy A and B sites in ZnFe<sub>2</sub>O<sub>4</sub> structure, respectively. We should pay attention to the intensity of peak O in M-900 is stronger than M-1200, indicating that when temperature goes up some Zn atoms enter into A sites from B sites, namely equal Fe atoms migrate to the opposite direction. Further conclusion is ZnFe<sub>2</sub>O<sub>4</sub> formed in 1200 °C have more ordered structure with the growth of crystals and improvement of crystallinity. According to previous reports [49,51], higher temperature always induced a more ordered spinel structure for ZnFe<sub>2</sub>O<sub>4</sub> nanoparticles, which can be explained by the structural adjustment and optimization under high temperature. As for ZnO, there is only one type of coordination polyhedron in its lattice structure, so the changes of cation occupancy in ZnO would not proceed. In consequence, it is convinced that the contribution of ZnO in XANES of M-900 and M-1200 are the same as that of pure ZnO (black dashed line in Fig. 8) although they are overlapped by the spectra of ZnFe<sub>2</sub>O<sub>4</sub>. The only cause of the spectral discrepancy between M-900 and M-1200 must from the cation configuration of ZnFe<sub>2</sub>O<sub>4</sub>.

Moreover, the cations migration and lattice defects can evoke significant changes in the symmetry vibrations, which are sensitive to Raman detection. The Raman spectra of M-900 and M-1200, as well as vibration modes of pure ZnO and ZnFe<sub>2</sub>O<sub>4</sub> are shown in Fig. 9. The bands appeared at 102, 208, 334, 379, 410, 437, 577 and 592 cm<sup>-1</sup> can be assigned to the first or second order Raman scattering in ZnO [52–54]. And ZnFe<sub>2</sub>O<sub>4</sub> have five Raman active modes, centered at 221, 246, 355, 451 and 647 cm<sup>-1</sup> [54,55]. Therefore, the Raman spectra of M-900 and M-1200 contain almost all the vibration modes of ZnO and one remarkable mode of ZnFe<sub>2</sub>O<sub>4</sub>, demonstrating the samples only contain these two mineral phases. Especially, we still focus on ZnFe<sub>2</sub>O<sub>4</sub> that acts as the probe of structure adjustment in our case. The band at 644 cm<sup>-1</sup> is assigned as A<sub>1g</sub> type of ZnFe<sub>2</sub>O<sub>4</sub>, attributed to the oxygen breathing vibrations against metal cations in tetrahedral AO<sub>4</sub> groups, while the rest lower frequency modes are interpreted in the octahedral BO<sub>6</sub> sites of ZnFe<sub>2</sub>O<sub>4</sub> [56]. In particular, when the cations distribute disorderly, the vibration mode relating to Zn and Fe atoms at AO<sub>4</sub> sites

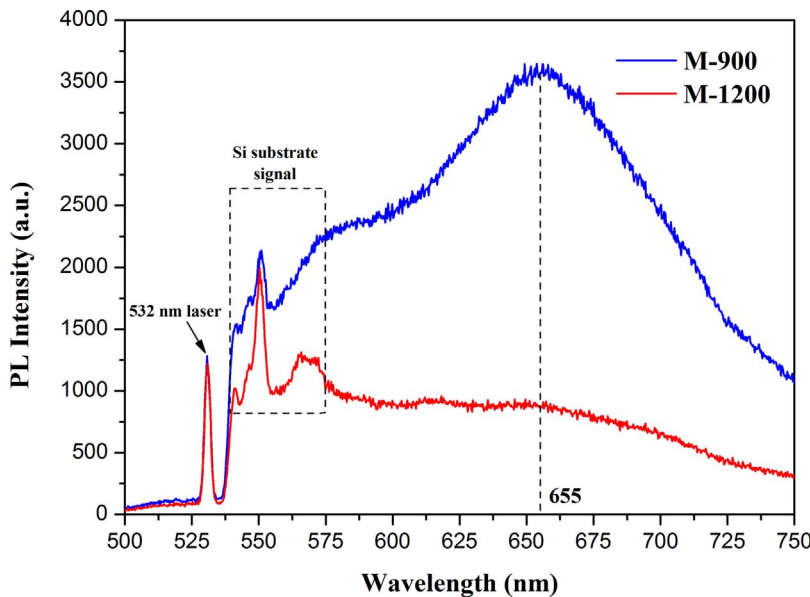


**Fig. 10.** PL spectra of M-900 and M-1200 under 532 nm laser excitation. The broad peak ranged from 600 to 725 nm (centered at 655 nm) is the PL signal of  $\text{ZnFe}_2\text{O}_4$  in M-900. Other sharp peaks appeared below 580 nm can be assigned as the signals of silicon substrate and laser, as labeled in the Figure.

( $644 \text{ cm}^{-1}$ ) of  $\text{ZnFe}_2\text{O}_4$  may split into two approaching peaks, thus exhibiting an overlapped broad peak [54]. Therefore, we can conclude that the cations in  $\text{ZnFe}_2\text{O}_4$  of M-900 are disordered, where A and B sites are randomly filled with Fe and Zn atoms. In comparison,  $\text{ZnFe}_2\text{O}_4$  in M-1200 displays a sharper band in the same position, resulting from the distribution of cations becomes ordered and the repair of antisite defects happens under higher temperature.

Based on the above analyses, we know that the thermal modification mainly influences the distribution of cations in the spinel structure of  $\text{ZnFe}_2\text{O}_4$ . When  $\text{ZnFe}_2\text{O}_4$  nanoparticles initially form at around  $800^\circ\text{C}$ , Zn and Fe atoms randomly distribute in tetrahedral and octahedral sites. The formed antisite defects induce non-equilibrium and unsteady states in  $\text{ZnFe}_2\text{O}_4$  [51]. Improving the temperature benefits the redistribution of Zn and Fe atoms in  $\text{ZnFe}_2\text{O}_4$  and promote the growth of  $\text{ZnO}/\text{ZnFe}_2\text{O}_4$  grain crystals, therefore leading to the transformation towards more ordered and stable states with less defects.

Further insight into the photogenerated charges property of M-900 and M-1200 is illustrated by the PL spectra (Fig. 10). Since  $\text{ZnO}$  is UV-responsive, we used the green laser ( $532 \text{ nm}$ ) to only excite the intrinsic and defect-related transitions of  $\text{ZnFe}_2\text{O}_4$ . M-900 exhibits a broad and intense PL band ranging from 600 to  $750 \text{ nm}$ . The structural defects in crystal lattice may serve as the recombination sites of photo-generated  $e^-$  and  $h^+$  [57]. Thus the PL emissions from M-900 are probably owing to the trapping of excitons by intrinsic radiative recombination ( $655 \text{ nm}$ ) or defects of  $\text{ZnFe}_2\text{O}_4$ . By contrast, the PL signal of M-1200 keeps silent, which is probably due to the formation of ordered structure and the repair of antisite defects that avoiding the defects recombination. In addition, the formation of  $\text{ZnO}/\text{ZnFe}_2\text{O}_4$  coupled semiconductor also greatly weakens the intrinsic radiative recombination, which infers that M-1200 have generated a steady and efficient photocatalysis system. Therefore, the lifetime of photogenerated carriers in M-1200 is prolonged, and its photocatalytic efficiencies towards the degradation of MO and the disinfection of *E. coli* K-12 are consequently improved. Above all, the optimization of structure is very helpful to improve the photocatalytic activity, which should be the chief principle to fabricate new mineral-based photocatalysts.

### 3.5. Enhanced electron-holes separation efficiency of $\text{ZnO}/\text{ZnFe}_2\text{O}_4$ coupled photocatalyst as evaluated by IPCE

The UV-vis DRS shows that both M-1200 and M-0 are sensitive to almost the whole wavelength range of visible light, and thus can be

excited out roughly equal numbers of photo-generated electrons and holes if provided with the same irradiation condition. Therefore, their photocatalytic activities should be mainly affected by the separation efficiency of electrons and holes.

We use IPCE to compare the photon-electron transfer efficiency of M-0 and M-1200 (Fig. 11). Six different wavelengths of visible light ( $416, 467, 524, 565, 616$  and  $680 \text{ nm}$ ) were chosen for conducting the photoelectrochemical experiments and IPCE calculation. The results clearly show that the IPCE profiles of both samples show good coordination with the light absorption spectra (Fig. 6). Increasing the light wavelength results in weaker optical absorption and thus lowers the photon-electron conversion efficiency. Therefore, the IPCE of both samples diminish with rising wavelength. At each fixed wavelength, the IPCE values of M-1200 are much higher ( $0.66\%, 0.36\%, 0.27\%, 0.18\%, 0.14\%$  and  $0.18\%$  at wavelength of  $416, 467, 524, 565, 616$  and  $680 \text{ nm}$ , respectively) than those of M-0 ( $0.19\%, 0.11\%, 0.09\%, 0.07\%, 0.08\%$  and  $0.08\%$ , respectively). This could be due to the more efficient separation of electron-hole pairs in coupled photocatalyst  $\text{ZnO}/\text{ZnFe}_2\text{O}_4$ . Totally, the photon-electron conversion efficiency of M-1200 is calculated to be up to 2.5 times higher than M-0 in the whole wavelength range of visible light. Actually, natural (Zn, Fe)S has been proved to be a laudable visible-light photocatalyst according to several literature [21–25], but the coupled  $\text{ZnO}/\text{ZnFe}_2\text{O}_4$  now exhibits striking out performance than its raw material.

Compared with the mechanical mixed sample and M-900, the intimate intergrowth of  $\text{ZnO}$  and  $\text{ZnFe}_2\text{O}_4$ , and accordingly, the steady establishment of coupled semiconductor system in M-1200 sample are suggested to be essential to enhance the visible-light photocatalytic performance. At aqueous pH level of 7.0, the valence and conduction band edges of  $\text{ZnFe}_2\text{O}_4$  are located at ca.  $0.38 \text{ V}$  and  $-1.54 \text{ V}$  vs. NHE, respectively; and the valence and conduction band edges of  $\text{ZnO}$  are located at ca.  $2.7 \text{ V}$  and  $-0.5 \text{ V}$  vs. NHE, respectively [58,59]. Obviously, the conduction and valance band edges of  $\text{ZnFe}_2\text{O}_4$  are more negative than those of  $\text{ZnO}$ , illustrated schematically in Fig. 12. The energy level difference between these two semiconductors can cause photo-generated carriers flow spontaneously instead of recombining immediately, which effectively promotes the separation of photo-generated electron and hole pairs on the surface of semiconductor. More importantly, this kind of band alignment with a visible-light excited semiconductor member can effectively improve solar energy utilization efficiency. According to our previous researches [22,24,25], photo-electrons ( $e^-$ ) is responsible for reductive degradation of MO dye and

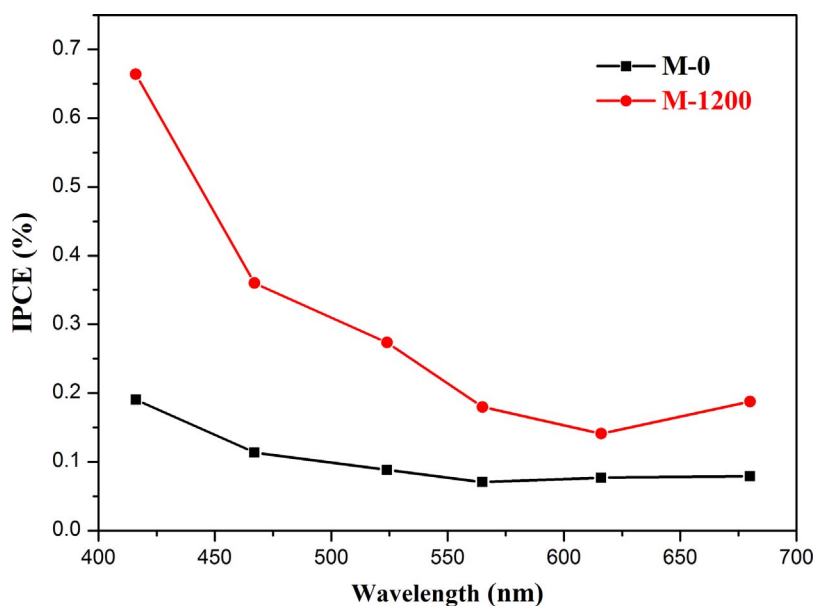


Fig. 11. IPCE curves for M-0 and M-1200 under different wavelengths of visible light.

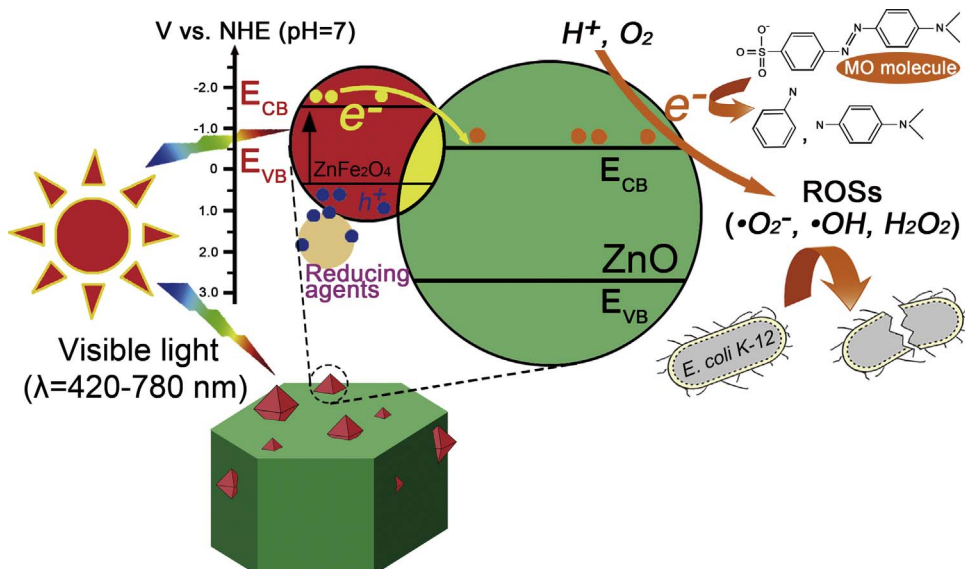


Fig. 12. Schematic illustration of photocatalytic mechanism of fabricated ZnO/ZnFe<sub>2</sub>O<sub>4</sub>.

ROSSs (reactive oxidative species) such as hydrogen peroxide (H<sub>2</sub>O<sub>2</sub>), hydroxyl radical (•OH) and the superoxide radical (•O<sub>2</sub><sup>-</sup>) get involved in inactivating *E. coli* K-12. Considering the existence of energy-level difference, we can hypothesize that when visible light strikes the ZnO/ZnFe<sub>2</sub>O<sub>4</sub> system, e<sup>-</sup> is injected into the conduction band of ZnO from more negative conduction band of excited ZnFe<sub>2</sub>O<sub>4</sub>, and then react with MO or kill the bacteria via the form of e<sup>-</sup> itself or ROSSs intermediates. At the same time, the photo-generated holes on the ZnFe<sub>2</sub>O<sub>4</sub> surface are scavenged by reducing agents in solution such as H<sub>2</sub>O or added ascorbic acid molecules (shown in Fig. 12). In conclusion, the fabricated coupled ZnO/ZnFe<sub>2</sub>O<sub>4</sub> can utilize visible light to finish photocatalytic degradation of azo-dye and bacterial disinfection, which is benefited from the high separation efficiency and long lifetime of photogenerated electron-hole pairs, and gaining an enormous advantage over natural sample in kinetics.

### 3.6. Prospect on mineral-based photocatalysts

Earth today boasts about more than 5300 known species of minerals with over 50 new types being identified each year (<http://rruff.info/>

ima), which have established a gigantic natural database of nearly all inorganic materials and some organic materials. Besides the Earth-abundant, low-cost and easy available properties of natural minerals, the diversity of chemical compositions, phase components and crystal structures makes them versatile in application, even further inspires scientists to fabricate new functional materials for broader industrial and scientific purposes. Factually, minerals have been recognized as environmental “cleaners” in nature over a long geological time [60–62]. The utilization of mineral-base materials to solve environmental problems, to some extent, conform the laws of nature. It not only improves the utilizing level of natural mineral resources, but also promotes the large-scale application of some related environmental technology.

In terms of semiconductor photocatalysis, the inherent impurities and defects of natural minerals endow themselves with outstanding solar-responsive capability, but also make them often with less satisfactory photocatalytic effects as compared with their synthetic counterparts. Fabrication of new semiconductors from natural raw mineral materials is a simple and easy-going solution. Just as evidenced by our work, the ZnO/ZnFe<sub>2</sub>O<sub>4</sub> coupled photocatalyst fabricated from

the calcination of natural sphalerite performs significantly enhanced charge separation efficiency and improved photocatalytic activity. Based on this idea, for example, calcining paragenetic sulfide minerals such as chalcopyrite ( $\text{CuFeS}_2$ ) and bornite ( $\text{Cu}_5\text{FeS}_4$ ) might form a  $\text{CuO}-\text{Cu}_2\text{O}-\text{Fe}_2\text{O}_3$  ternary semiconductor, and  $\text{Cu}_2\text{O}/\text{Fe}_2\text{O}_3$  has been confirmed as a composite photocatalyst for  $\text{CO}_2$  photoconduction under visible light [63]. Surface oxidation of pyrite could produce hematite ( $\text{Fe}_2\text{O}_3$ )/pyrite ( $\text{FeS}_2$ ) binary semiconductor to split water, which was thought to have existed in both early Earth and Mars [64]. Partly oxidizing Cd-bearing sphalerite could give rise to  $\text{CdS}/\text{ZnO}$  coupled semiconductor, which has been reported to achieve a maximal IPCE of 18.6% [65]. Besides, in a certain amount of ore deposits, different types of semiconducting minerals are paragenetic. For example, sulfides of galena ( $\text{PbS}$ ), sphalerite ( $\text{ZnS}$ ), greenockite ( $\text{CdS}$ ) and pyrite ( $\text{FeS}_2$ ) are always born to be associated with each other. After proper modification, they can be made into multiform of composite photocatalysts and realize satisfying photocatalytic effects. However, in order to obtain the optimized photocatalytic efficiency, according to this study, optimizing the phase components, phase ratio, lattice structure and energy band configuration are of vital importance.

#### 4. Conclusion

We have successfully fabricated  $\text{ZnO}/\text{ZnFe}_2\text{O}_4$  coupled photocatalyst by utilizing natural, Earth-abundant and low-cost Fe-bearing sphalerite ((Zn, Fe)S) in a very simple heating procedure. The  $\text{ZnO}/\text{ZnFe}_2\text{O}_4$  coupled photocatalyst performs enhanced photoresponse to visible light and improved photocatalytic activity to remove MO and inhibit *E. coli* as compared with the original mineral sample. The enhanced visible-light photocatalytic activity benefits from the formation of coupled binary semiconductor with advantageous band alignment, which help to improve the separation efficiency of photo-generated electron-hole pairs and largely prolong the lifetime of photoelectrons. Besides, more ordered spinel structure of  $\text{ZnFe}_2\text{O}_4$  forms at higher temperature, causing lower recombination probability of electrons and holes. So phase component, phase ratio, lattice structure and energy band configuration are crucial to promote photocatalytic performance. This work provides a facile and creative way to use Earth-abundant, environmental friendly and low-cost natural mineral-based photocatalysts to deal with practical environmental issues.

#### Acknowledgements

This research was supported by the National Basic Research Program of China (Program No. 2014CB846001), the Natural Science Foundation of China (Grant No. 41230103, 41272003, 42522201 & 41573086). Many thanks for the help from beamline staff in 4W1B of Beijing Synchrotron Radiation Facility and 06ID-1 and 06ID-1 of Canadian Light Source on XAFS measurements and data processing.

#### Appendix A. Supplementary data

Supplementary data associated with this article can be found, in the online version, at <https://doi.org/10.1016/j.apcatb.2017.12.051>.

#### References

- [1] A. Fujishima, K. Honda, Electrochemical photolysis of water at a semiconductor electrode, *Nature* 238 (1972) 37–38.
- [2] J.M. Herrmann, Heterogeneous photocatalysis: fundamentals and applications to the removal of various types of aqueous pollutants, *Catal. Today* 53 (1999) 115–129.
- [3] D.S. Bhatkhande, V.G. Pangarkar, A.A. Beenackers, Photocatalytic degradation for environmental applications—a review, *J. Chem. Technol. Biotechnol.* 77 (2002) 102–116.
- [4] C. Chen, W. Ma, J. Zhao, Semiconductor-mediated photodegradation of pollutants under visible-light irradiation, *Chem. Soc. Rev.* 39 (2010) 4206–4219.
- [5] M. Pelaez, N.T. Nolan, S.C. Pillai, M.K. Seery, P. Falaras, A.G. Kontos, P.S.M. Dunlop, J.W.J. Hamilton, J.A. Byrne, K. O’shea, M.H. Entezari, D.D. Dionysiou, A review on the visible light active titanium dioxide photocatalysts for environmental applications, *Appl. Catal. B: Environ.* 125 (2012) 331–349.
- [6] Y.P. Yuan, L.W. Ruan, J. Barber, S.C.J. Loo, C. Xue, Hetero-nanostructured suspended photocatalysts for solar-to-fuel conversion, *Energy Environ. Sci.* 7 (2014) 3934–3951.
- [7] S. Kim, S.J. Hwang, W. Choi, Visible light active platinum-ion-doped  $\text{TiO}_2$  photocatalyst, *J. Phys. Chem. B* 109 (2005) 24260–24267.
- [8] A. Iwase, H. Kato, A. Kudo, Nanosized Au particles as an efficient cocatalyst for photocatalytic overall water splitting, *Catal. Lett.* 108 (2006) 7–10.
- [9] J. Kiwi, E. Borgarello, E. Pelizzetti, M. Visca, M. Grätzel, Cyclic water cleavage by visible light: drastic improvement of yield of  $\text{H}_2$  and  $\text{O}_2$  with bifunctional redox catalysts, *Angew. Chem. Int. Ed.* 19 (1980) 646–648.
- [10] T. Sano, S. Kutsuna, N. Negishi, K. Takeuchi, Effect of Pd-photodeposition over  $\text{TiO}_2$  on product selectivity in photocatalytic degradation of vinyl chloride monomer, *J. Mol. Catal. A: Chem.* 189 (2002) 263–270.
- [11] S. Rengaraj, X.Z. Li, Enhanced photocatalytic activity of  $\text{TiO}_2$  by doping with Ag for degradation of 2, 4, 6-trichlorophenol in aqueous suspension, *J. Mol. Catal. A: Chem.* 243 (2006) 60–67.
- [12] R. Konta, T. Ishii, H. Kato, A. Kudo, Photocatalytic activities of noble metal ion doped  $\text{SrTiO}_3$  under visible light irradiation, *J. Phys. Chem. B* 108 (2004) 8992–8995.
- [13] Y. Xu, M.A.A. Schoonen, The absolute energy positions of conduction and valence bands of selected semiconducting minerals, *Am. Mineral.* 85 (2000) 543–556.
- [14] S.D. Scott, H.L. Barnes, Sphalerite geothermometry and geobarometry, *Econ. Geol.* 66 (1971) 653–669.
- [15] A. Lu, Y. Li, M. Lv, C. Wang, L. Yang, J. Liu, Y. Wang, K.H. Wong, P.K. Wong, Photocatalytic oxidation of methyl orange by natural V-bearing rutile under visible light, *Sol. Energy Mater. Sol. Cells* 91 (2007) 1849–1855.
- [16] D. Xia, Z. Shen, G. Huang, W. Wang, J.C. Yu, P.K. Wong, Red phosphorus: an earth-abundant elemental photocatalyst for green bacterial inactivation under visible light, *Environ. Sci. Technol.* 49 (2015) 6264–6273.
- [17] J. Zhang, T. Liu, R. Chen, X. Liu, Vermiculite as a natural silicate crystal for hydrogen generation from photocatalytic splitting of water under visible light, *RSC Adv.* 4 (2014) 406–408.
- [18] P. Qiu, T. Zhang, Y. Qiu, X. Shi, L. Chen, Sulfide bornite thermoelectric material: a natural mineral with ultralow thermal conductivity, *Energy Environ. Sci.* 7 (2014) 4000–4006.
- [19] Y. Li, A. Lu, C. Wang, X. Wu, Characterization of natural sphalerite as a novel visible light-driven photocatalyst, *Sol. Energy Mater. Sol. Cells* 92 (2008) 953–959.
- [20] Y. Li, A. Lu, C. Wang, Semiconducting mineralogical characteristics of natural sphalerite gestating visible-light photocatalysis, *Acta Geol. Sin. (English Ed.)* 83 (2009) 633–639.
- [21] Y. Li, A. Lu, C. Wang, Photocatalytic reduction of Cr(VI) by natural sphalerite suspensions under visible light irradiation, *Acta Geol. Sin. (English Ed.)* 80 (2006) 267–272.
- [22] Y. Li, A. Lu, S. Jin, C. Wang, Photo-reductive decolorization of an azo dye by natural sphalerite: case study of a new type of visible light-sensitized photocatalyst, *J. Hazard. Mater.* 170 (2009) 479–486.
- [23] X. Yang, Y. Li, A. Lu, Y. Yan, C. Wang, P.K. Wong, Photocatalytic reduction of carbon tetrachloride by natural sphalerite under visible light irradiation, *Sol. Energy Mater. Sol. Cells* 95 (2011) 1915–1921.
- [24] Y. Chen, T.W. Ng, A. Lu, Y. Li, H.Y. Yip, T. An, G. Li, H. Zhao, M. Gao, P.K. Wong, Comparative study of visible-light-driven photocatalytic inactivation of two different wastewater bacteria by natural sphalerite, *Chem. Eng. J.* 234 (2013) 43–48.
- [25] D. Xia, T.W. Ng, T. An, G. Li, Y. Li, H.Y. Yip, H. Zhao, A. Lu, P.K. Wong, A recyclable mineral catalyst for visible-light-driven photocatalytic inactivation of bacteria: natural magnetic sphalerite, *Environ. Sci. Technol.* 47 (2013) 11166–11173.
- [26] S.L. Harmer, A. Mierczynska-Vasilev, D.A. Beattie, J.G. Shapter, The effect of bulk iron concentration and heterogeneities on the copper activation of sphalerite, *Miner. Eng.* 21 (2008) 1005–1012.
- [27] S.H. Deulkar, C.H. Bhosale, M. Sharon, Effect of Fe substitution on optical electrical, electrochemical and dielectric properties of (Zn, Fe)S chalcogenide pellets, *Mater. Chem. Phys.* 89 (2005) 211–215.
- [28] H.L. Liu, T.C.K. Yang, Photocatalytic inactivation of *Escherichia coli* and *Lactobacillus helveticus* by  $\text{ZnO}$  and  $\text{TiO}_2$  activated with ultraviolet light, *Process Biochem.* 39 (2003) 475–481.
- [29] R.I. Dimitrov, N. Moldovanska, I.K. Bonev, Ž. Živkovic, Oxidation of marmatite, *Thermochim. Acta* 362 (2000) 145–151.
- [30] T.T. Chen, J.E. Dutrizac, Mineralogical changes occurring during the fluid-bed roasting of zinc sulfide concentrates, *JOM* 56 (2004) 46–51.
- [31] X. Guo, H. Zhu, Q. Li, Visible-light-driven photocatalytic properties of  $\text{ZnO}/\text{ZnFe}_2\text{O}_4$  core/shell nanocable arrays, *Appl. Catal. B: Environ.* 160 (2014) 408–414.
- [32] Y. Bu, Z. Chen, W. Li, A  $\text{ZnFe}_2\text{O}_4-\text{ZnO}$  nanorod array p-n junction composite and its photoelectrochemical performance, *Dalton Trans.* 42 (2013) 16272–16275.
- [33] D.D. Qin, C.L. Tao, A nanostructured  $\text{ZnO}-\text{ZnFe}_2\text{O}_4$  heterojunction for the visible light photoelectrochemical oxidation of water, *RSC Adv.* 4 (2014) 16968–16972.
- [34] J. Hu, Y. Xie, X. Zhou, J. Yang, Solid-state synthesis of  $\text{ZnO}$  and  $\text{ZnFe}_2\text{O}_4$  to form p-n junction composite in the use of dye sensitized solar cells, *J. Alloys Compd.* 676 (2016) 320–325.
- [35] I.C. Madsen, N.V. Scarlett, L.M. Cranswick, T. Lwin, Outcomes of the International Union of Crystallography Commission on powder diffraction round robin on quantitative phase analysis: samples 1a to 1h, *J. Appl. Crystallogr.* 34 (2001) 409–426.
- [36] N.V. Scarlett, I.C. Madsen, L.M. Cranswick, T. Lwin, E. Groleau, G. Stephenson, M. Aylmore, N. Agron-Olshina, Outcomes of the international union of

- crystallography commission on powder diffraction round robin on quantitative phase analysis: samples 2, 3, 4, synthetic bauxite, natural granodiorite and pharmaceuticals, *J. Appl. Crystallogr.* 35 (2002) 383–400.
- [37] M. Newville, IFEFFIT: interactive XAFS analysis and FEFF fitting, *J. Synchrotron Radiat.* 8 (2001) 322–324.
- [38] J.M. Macák, H. Tsuchiya, A. Ghicov, P. Schmuki, Dye-sensitized anodic TiO<sub>2</sub> nanotubes, *Electrochem. Commun.* 7 (2005) 1133–1137.
- [39] G.C. Allen, M. Paul, Chemical characterization of transition metal spinel-type oxides by infrared spectroscopy, *Appl. Spectrosc.* 49 (1995) 451–458.
- [40] G.M. Schwab, J. Philinis, Reactions of iron pyrite: its thermal decomposition, reduction by hydrogen and air oxidation, *J. Am. Chem. Soc.* 69 (1947) 2588–2596.
- [41] D.A. Cole, G.W. Simmons, R.G. Herman, K. Klier, I. Czakó-Nagy, Transformations of iron minerals during coal oxidation, *Fuel* 66 (1987) 1240–1248.
- [42] N.A. Warner, T.R. Ingraham, Decomposition pressures of ferric sulphate and aluminium sulphate, *Can. J. Chem.* 38 (1960) 2196–2202.
- [43] G. Hu, K. Dam-Johansen, S. Wedel, J.P. Hansen, Decomposition and oxidation of pyrite, *Prog. Energy Combust. Sci.* 32 (2006) 295–314.
- [44] J.W. Graydon, D.W. Kirk, A microscopic study of the transformation of sphalerite particles during the roasting of zinc concentrate, *Metall. Trans. B* 19 (1988) 141–146.
- [45] V. Srikanth, D.R. Clarke, On the optical band gap of zinc oxide, *J. Appl. Phys.* 83 (1998) 5447–5451.
- [46] E. Casbeer, V.K. Sharma, X.Z. Li, Synthesis and photocatalytic activity of ferrites under visible light: a review, *Sep. Purif. Technol.* 87 (2012) 1–14.
- [47] A. Manikandan, J.J. Vijaya, M. Sundararajan, C. Meganathan, L.J. Kennedy, M. Bououdina, Optical and magnetic properties of Mg-doped ZnFe<sub>2</sub>O<sub>4</sub> nanoparticles prepared by rapid microwave combustion method, *Superlattices Microstruct.* 64 (2013) 118–131.
- [48] A. Manikandan, J.J. Vijaya, L.J. Kennedy, M. Bououdina, Structural, optical and magnetic properties of Zn<sub>1-x</sub>Cu<sub>x</sub>Fe<sub>2</sub>O<sub>4</sub> nanoparticles prepared by microwave combustion method, *J. Mol. Struct.* 1035 (2013) 332–340.
- [49] S. Nakashima, K. Fujita, K. Tanaka, K. Hirao, T. Yamamoto, I. Tanaka, First-principles XANES simulations of spinel zinc ferrite with a disordered cation distribution, *Phys. Rev. B* 75 (2007) 174443.
- [50] S.J.A. Figueroa, S.J. Stewart, First XANES evidence of a disorder-order transition in a spinel ferrite compound: nanocrystalline ZnFe<sub>2</sub>O<sub>4</sub>, *J. Synchrotron Radiat.* 16 (2009) 63–68.
- [51] A. Šutka, R. Párná, M. Zamovskis, V. Kisand, G. Mezinskis, J. Kleperis, M. Maiorov, D. Jakovlev, Effect of antisite defects on the magnetic properties of ZnFe<sub>2</sub>O<sub>4</sub>, *Phys. Status Solidi (A)* 210 (2013) 1892–1897.
- [52] J. Serrano, A.H. Romero, F.J. Manjón, R. Lauck, M. Cardona, A. Rubio, Pressure dependence of the lattice dynamics of ZnO: an ab initio approach, *Phys. Rev. B* 69 (2004) 094306.
- [53] R. Cuscó, E. Alarcón-Lladó, J. Ibáñez, L. Artús, J. Jiménez, B. Wang, M.J. Callahan, Temperature dependence of Raman scattering in ZnO, *Phys. Rev. B* 75 (2007) 165202.
- [54] N. Romcevic, R. Kostic, M. Momcevic, B. Hadzic, I. Kurylisyn-Kudelska, W. Dobrowolski, U. Narkiewicz, D. Siber, Raman scattering from ZnO (Fe) nanoparticles, *Acta Phys. Pol. A* 114 (2008) 1323–1328.
- [55] Z. Wang, D. Schiferl, Y. Zhao, H.S.C. O'Neill, High pressure Raman spectroscopy of spinel-type ferrite ZnFe<sub>2</sub>O<sub>4</sub>, *J. Phys. Chem. Solids* 64 (2003) 2517–2523.
- [56] M. Maletin, E.G. Moshopoulou, A.G. Kontos, E. Devlin, A. Delimitis, V.T. Zaspalis, L. Nalbandian, V.V. Srdic, Synthesis and structural characterization of in-doped ZnFe<sub>2</sub>O<sub>4</sub> nanoparticles, *J. Eur. Ceram. Soc.* 27 (2007) 4391–4394.
- [57] X. Chen, S. Shen, L. Guo, S.S. Mao, Semiconductor-based photocatalytic hydrogen generation, *Chem. Rev.* 110 (2010) 6503.
- [58] G. Redmond, A. Okeeffe, C. Burgess, C. MacHale, D. Fitzmaurice, Spectroscopic determination of the flatband potential of transparent nanocrystalline ZnO films, *J. Phys. Chem.* 97 (1993) 11081–11086.
- [59] S. Boumaza, A. Boudjemaa, A. Bouguelia, R. Bouarab, M. Trari, Visible light induced hydrogen evolution on new hetero-system ZnFe<sub>2</sub>O<sub>4</sub>/SrTiO<sub>3</sub>, *Appl. Energy* 87 (2010) 2230–2236.
- [60] D.J. Vaughan, R.A.D. Patrick, R.A. Wogelius, Minerals, metals and molecules: ore and environmental mineralogy in the new millennium, *Mineral. Mag.* 66 (2002) 653–676.
- [61] D.J. Vaughan, J.R. Lloyd, Mineral-organic-microbe interactions: environmental impacts from molecular to macroscopic scales, *C.R. Geosci.* 343 (2011) 140–159.
- [62] G.E. Brown, G. Calas, Environmental mineralogy—understanding element behavior in ecosystems, *C.R. Geosci.* 343 (2011) 90–112.
- [63] J.C. Wang, L. Zhang, W.X. Fang, J. Ren, Y.Y. Li, H.C. Yao, Z.J. Li, Enhanced photoreduction CO<sub>2</sub> activity over direct Z-scheme α-Fe<sub>2</sub>O<sub>3</sub>/Cu<sub>2</sub>O heterostructures under visible light irradiation, *ACS Appl. Mater. Interfaces* 7 (2015) 8631–8639.
- [64] C.M. Eggleston, J.R. Stern, T.M. Strelitz, B.A. Parkinson, A natural photoelectrochemical cell for water splitting: implications for early Earth and Mars, *Am. Mineral.* 97 (2015) 1804–1807.
- [65] W. Lee, S.K. Min, V. Dhas, S.B. Ogale, S.H. Han, Chemical bath deposition of CdS quantum dots on vertically aligned ZnO nanorods for quantum dots-sensitized solar cells, *Electrochem. Commun.* 11 (2009) 103–106.